Modeling and Incorporation of System Response Functions in 3-D Whole Body PET

Adam M. Alessio*, *Member, IEEE*, Paul E. Kinahan, *Senior Member, IEEE*, and Thomas K. Lewellen, *Senior Member, IEEE*

***Abstract*—Appropriate application of spatially variant system models can correct for degraded resolution response and mispositioning errors. This paper explores the detector blurring component of the system model for a whole body positron emission tomography (PET) system and extends this factor into a more general system response function to account for other system effects including the influence of Fourier rebinning (FORE). We model the system response function as a three-dimensional (3-D) function that blurs in the radial and axial dimension and is spatially variant in radial location. This function is derived from Monte Carlo simulations and incorporates inter-crystal scatter, crystal penetration, and the blurring due to the FORE algorithm. The improved system model is applied in a modified ordered subsets expectation maximization (OSEM) algorithm to reconstruct images from rebinned, fully 3-D PET data. The proposed method effectively removes the spatial variance in the resolution response, as shown in simulations of point sources. Furthermore, simulation and measured studies show the proposed method improves quantitative accuracy with a reduction in tumor bias compared to conventional OSEM on the order of 10%–30% depending on tumor size and smoothing parameter.**

***Index Terms*—Detector response, Fourier rebinning (FORE), fully three-dimensional (3-D) positron emission tomography (PET), system model, system response.**

I. Introduction

POSITRON emission tomography (PET) is finding increasing applications in oncology imaging because of its ability to provide quantitative information about biological processes. Modern PET scanners continue to improve through advances in electronics, detectors, and data processing to overcome a variety of physical limitations. One of the challenges facing these tomographs is their spatially variant resolution response. Fig. 1 plots the two-dimensional (2-D) full-width at half-maximum (FWHM) for a point source as a function of the distance from the center of the tomograph and highlights the variant resolution response present in whole-body scanners. These plots were generated from Monte Carlo simulations of a system with a geometry similar to the GE Advance scanner [1] and from filtered back projection (FBP) reconstructions using a ramp filter. The top row of Fig. 1 plots a radial profile through three sinograms of point sources at three different radial positions in the scanner. The second row plots a profile through the image reconstructed from these sinograms. Clearly, the sinogram response and image point spread function varies based on location in the scanner. Similarly, the mispositioning errors are greater at the edge of the field of view (FOV) due to more inter-crystal scatter in the angled detectors at the edge of the circular detector ring.

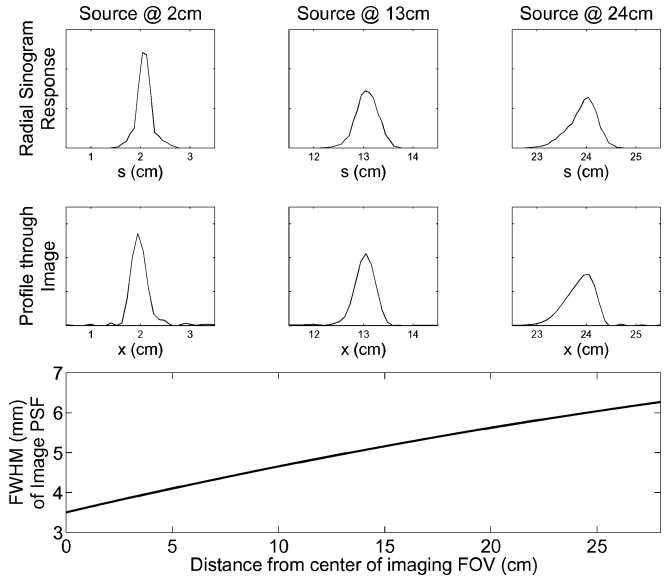

Fig. 1. Transaxial resolution as a function of distance from center of tomograph revealing the spatially variant resolution response of PET systems. Top row plots the radial profile through a sinogram formed at varying radial locations. Second row plots horizontal profiles through the points in the reconstructed image. Third row plots the average FWHM of the point spread function in the image domain as a function of radial location.

Improvements in computing speed and hardware implementations of software have allowed previously time-consuming iterative reconstruction algorithms to become standard protocol on many systems. These iterative methods are beneficial because they can accurately model noise and system effects. Despite this potential, most image reconstruction methods use spatially invariant system models which do not match the true system.

Spatially variant system models have been shown to be advantageous for high-resolution small animal PET systems [2]–[6]. Our previous work has shown resolution improvements in a small animal system for 2-D PET imaging [7], [8]. We showed that appropriate incorporation of spatially variant system models can correct for degraded, variant resolution response and mispositioning errors (particularly at the edge of the FOV). This paper explores the detector blurring component

Manuscript received September 1, 2005; revised February 20, 2006. This work was supported by the National Institutes of Health under Grant CA74135 and Grant CA42593. *Asterisk indicates corresponding author.*

*A. M. Alessio is with the Department of Radiology, University of Washington Medical Center, Seattle, WA 98195-6004 USA (e-mail: aalessio@u.washington.edu).

P. E. Kinahan and T. K. Lewellen are with the Department of Radiology, University of Washington Medical Center, Seattle, WA 98195-6004 USA.

Digital Object Identifier 10.1109/TMI.2006.873222

of the system model for a human, whole-body PET system and extends this factor into a more general system response function (SRF) to account for other system nonidealities such as the influence of Fourier rebinning (Fourier rebinning) [9] on fully three-dimensional (3-D) imaging. In an effort to improve reconstructions from Fourier rebinned PET data, we model the SRF as a 3-D function that blurs the standard geometric system model in the radial and axial dimensions and is spatially variant in radial location. We measure the SRF from Monte Carlo simulations and apply the new system model in a modified ordered subsets expectation maximization (OSEM) algorithm to reconstruct images with improved resolution and quantitative accuracy. The proposed method is tested with simulated and measured data sets containing clinically relevant noise levels to gauge expected improvements in a clinical setting.

II. Description of System Response Function

Many iterative reconstruction methods use only a simple, spatially invariant, geometric system model. This model relates a projection bin to its contributing voxels based solely on the intersection of lines (or tubes) of response and image elements. Spatially variant system models have been described in terms including coincident aperture functions [4], [10], detector response functions [11], or system kernels [2]. These different functions incorporate various system effects including inter-crystal scatter, crystal penetration, photon pair noncolinearity, and nonuniform sinogram sampling. We propose a more general blurring factor denoted as the SRF. The SRF modifies the simple geometric system model to account for system nonidealities.

In a fully determined system model, the SRF is unique for each detector pair and to each volume location that contributes to the pair. In fully 3-D PET, this equates to a seven-dimensional (7-D) function which can be described with four dimensions for the sinogram domain and three dimensions for the imaging volume domain. Fig. 2 illustrates the SRF $\mathbf{S}(u, w, \phi, \theta; x_v, y_v, z_v)$, where (u, w) defines the point on one detector surface where the coincident bin with azimuthal and axial angle (ϕ, θ) intersects. Point (x_v, y_v, z_v) defines the location in the image volume that contributes to this coincident bin.

The commonly used spatially invariant system models, that only describe the geometric features of the scanner and the effects of attenuation (for accurate Poisson statistical modeling [12]), do not account for numerous system nonidealities. The SRF for these simple models could be considered one-dimensional (1-D). Past efforts to model a spatially variant system blurring factor could be expressed with the 2-D function, $\mathbf{S}_{1+1}(s; s_v)$, which blurs along radial bins in the sinograms (s, the distance between the z axis and the projection of the line onto a transaxial plane) and is spatially variant in radial distance s_v. The subscript v denotes the variables that parameterize the originating volume location as opposed to the line integrals. With this notation, the top row of Fig. 1 plots the system response function $\mathbf{S}_{1+1}(s; s_v)$ and the second row plots a horizontal profile through a reconstructed point at varying s_v.

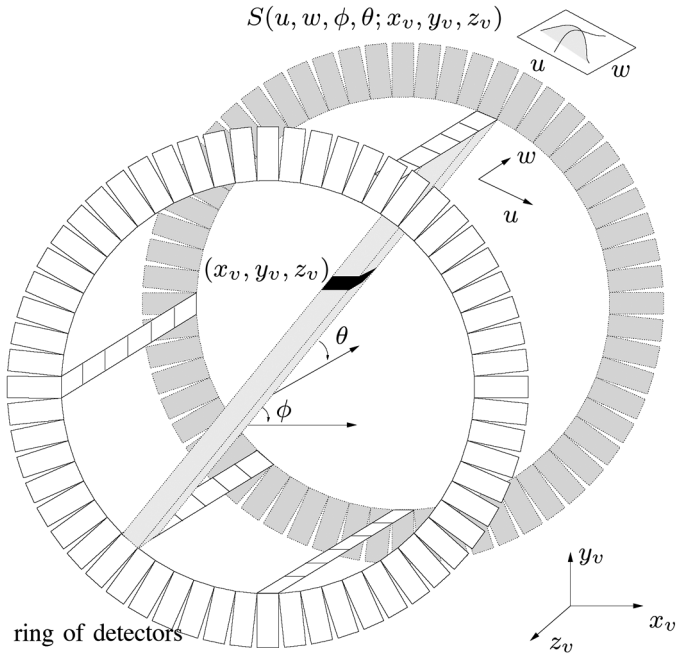

Fig. 2. Illustration of fully characterized system response function, $\mathbf{S}_{4+3}$, shows point (u, w) on one detector surface where the coincident bin with azimuthal and axial angle (ϕ, θ) intersects. Point (x_v, y_v, z_v) defines the location in the volume that contributes to this coincident bin.

We denote a fully characterized system response as $\mathbf{S}_{4+3}$ with the subscript "4 + 3" to denote that four dimensions describe the line integral domain (data domain) and three dimensions describe the originating volume. The use of this 7-D function is computationally infeasible both in terms of storage and computation time constraints. To simplify the implementation of the response function and improve reconstruction speed, we present a system response with reduced dimensionality. This work presents a 3-D function $\mathbf{S}_{2+1}(s, z; s_v)$, which blurs across radial bins (s) and axial planes (z) and is variant along the radial direction (s_v). This function incorporates the system effects of inter-crystal scatter, crystal penetration, and the blurring due to Fourier rebinning.

III. Acquiring the System Response Function

The system response function can be determined through analytical derivations [4], [13]–[15], with Monte Carlo simulations [3], [16], [17], or empirically [2], [8], [11], [18], [19]. In theory, the empirical approach of physically measuring the system response to a collimated point source leads to the most accurate description of the system. The experimental setup for these measurements can be challenging due to the need to precisely position the point source and the multiple degrees-of-freedom in the collimation. We employed a Monte Carlo simulation method [20] with the intention that it could be translated into a feasible empirical setup to accurately define the system model for a real scanner.

Using the SimSET simulation package modified to account for discrete detector elements, we simulated a whole-body PET scanner with a geometry and detection system similar to the GE Advance PET tomograph [1]. We positioned single point sources at different radial and axial locations in the imaging

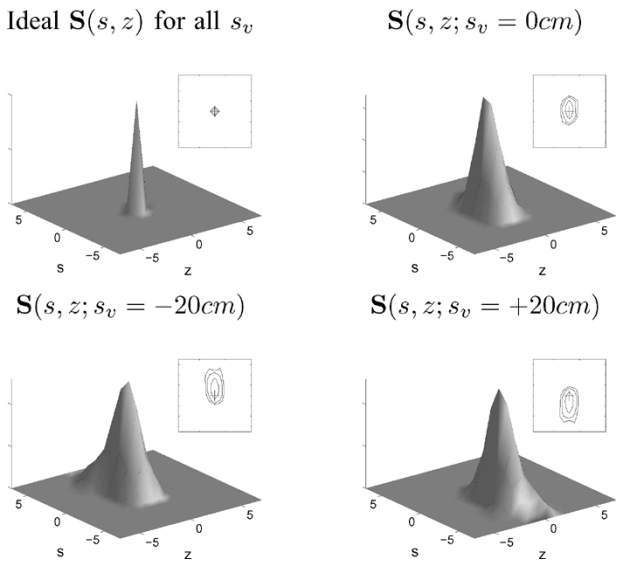

Fig. 3. $\mathbf{S}_{2+1}(s,z;s_v)$ at different radial locations s_v for transaxial FOV ($-$27.5 cm, 27.5 cm). Inset (s,z) contour plots mark the center of ideal with the cross and show half, fifth, and tenth maximum contours.

FOV and collected fully 3-D emission data. The dimensionless point sources were not collimated, making this a feasible approach for real data measurements. This approach does not allow for measuring blurring in the azimuthal angle dimension since a single point source will contribute to all azimuthal angles and it is not possible to decouple the ideal response from the azimuthal blurring. As a simple validation of this approach, we performed simulations of collimated point sources to confirm that this whole body system causes minimal blurring in azimuthal angle. Each fully 3-D data set was Fourier rebinned into 2-D PET data $y(s,\phi,z)$ to lead to a fast, practical reconstruction method. As expected, analysis of the rebinned sinograms showed that the system blurs the coincident lines formed from a single point source in all three dimensions of the rebinned data. These data showed that the ranking of greatest to least blurring occurs amongst radial bins, then axial bins, and finally azimuthal angle bins. Moreover, the radial positioning of the source followed by the axial positioning cause the greatest variations in the system response. To simplify the 7-D response, we choose to use a kernel that only blurs in radial and axial bins and is variant in radial location. Fig. 3 presents the $\mathbf{S}_{2+1}$ SRF at different radial locations. The $-$5,0, and 5 labels on the x and y axis mark the number of radial and axial bins away from the center of the kernel.

These simulations do not include the effects of positron range or annihilation acolinearity which, along with the need to use point sources of some finite size, will increase the extent of each kernel in empirically measured system responses. Therefore, these simulations will underestimate the size of the system response functions. An underestimation of the model will lead to more modest results. We assume that if the results are beneficial with this simulated model and evaluation, then results from a measured system response will be equally or more beneficial.

The following summary outlines the steps performed to find the 3-D $\mathbf{S}_{2+1}(s,z;s_v)$. Four fully 3-D data sets were simulated from a point source at four different radial positions ($s_v = [4,11,18,25]$cm) and Fourier rebinned into 2-D sinograms. For a fixed ϕ, the (s,z) view of this data is the projection view of the data, as opposed to a sinogram view, and provides the desired system response information. The four data sets lead to known response functions (s,z) at four radial positions s_v. The response functions at the remaining positive s_v are approximated by parameterizing the simulated (s,z) functions with 2-D discrete cosine transform coefficients. Then, a least-squares fit to a linear relationship amongst the coefficients from the four simulated response functions leads to coefficient values at all s_v. The inverse 2-D discrete cosine transform of the coefficients provides the complete $\mathbf{S}_{2+1}$ SRF for all positive radial locations. The SRF for the other half of the field of view is formed by reversing the radial blurring component ($\mathbf{S}_{2+1}(-s,z;-s_v) = \mathbf{S}_{2+1}(s,z;s_v)$) under the assumption of a symmetric response in each half of the transaxial field of view. In short, the complete SRF is formed from interpolation in discrete cosine space. This interpolation can not account for drastic variations in the model from one radial location to the next which will occur particularly at edges of detector blocks in a real system. But, this interpolation does capture the basic changes in model shape and the blurring extent of the model at each radial location. We propose that the benefit of only needing to measure a few response functions and interpolating these values outweighs the error in the system model at the edges of blocks.

IV. Application of the System Response Function

The SRF was incorporated into the system matrix in a modified version of the OSEM algorithm [21]. In OSEM, the system matrix is used in the forward and back projection steps. As stated previously, typical system matrices only contain geometric effects and attenuation. The modified system matrix $\hat{\mathbf{P}}$ for rebinned data is formed from the convolution of the SRF with the nonspatially variant, geometric system model $\mathbf{P}$. We present two variations to evaluate the benefits of adding dimensionality to the SRF. We apply the 2-D $\mathbf{S}_{1+1}$, which ignores the axial blurring component, in the form

$$\hat{\mathbf{P}}(s_v,\phi,z;x_v,y_v,z_v) = \sum_{s'} \mathbf{S}_{1+1}(s_v - s';s_v)\mathbf{P}(s',\phi,z;x_v,y_v,z_v). \quad (1)$$

We also apply the proposed 3-D $\mathbf{S}_{2+1}$ by modifying the system matrix as

$$\tilde{\mathbf{P}}(s_v,\phi,z;x_v,y_v,z_v) = \sum_{s'}\sum_{z'} \mathbf{S}_{2+1}(s_v - s', z - z';s_v)\mathbf{P}(s',\phi,z';x_v,y_v,z_v). \quad (2)$$

One possible approach for including a SRF is to use a factorized model and apply this blurring term in the forward and back projector for each call to the system matrix, requiring a 2-D convolution every time the system matrix is accessed [16]. Another option, employed in our version of the algorithm, is to precompute the sparse blurred system matrix and store only the nonzero entries. The applied $\mathbf{S}_{2+1}$ blurring function consisted of a 9×5 kernel that varied at all radial bin positions.

Conventional 2-D OSEM performs a complete reconstruction of one transaxial plane then reconstructs the next transaxial plane. With the $\mathbf{S}_{2+1}$ SRF, the projections of the current image

estimate requires image estimates from the current plane and neighboring planes. Therefore, the algorithm was modified to perform one iteration on a plane then one iteration on the next plane. After performing one iteration on each slice, the algorithm starts over again and performs another pass through all slices.

V. Methods

A. Monte Carlo Simulations

We tested the incorporation of the 2-D and 3-D SRF with two separate simulation studies. First, we preformed Monte Carlo simulations of a phantom containing 17 dimensionless point sources at three different radial positions in the FOV. The fully 3-D Monte Carlo generated data were rebinned with FORE and reconstructed with ramp-filtered FBP, conventional OSEM, and OSEM with our improved system response functions to gauge the resolution improvements with the new method. The OSEM reconstructions used 12 subsets and nine iterations and no postsmoothing.

These simulations were designed to determine how the resolution changes throughout the field of view with the proposed methods. For this purpose, we used the metric of volume at half-maximum (VHM) defined as the volume of each reconstructed point with values greater than half of the point's maximum value. Similarly, we find the radius of the sphere inscribed in the half and tenth maximum values in each point. We also found the average transaxial FWHM and full-width at tenth-maximum (FWTM) versus the radial distance from the center of the FOV for the different reconstruction methods. The terms are calculated from the average FWHM (and FWTM) of all the points at a given radius in the image. The FWHM of a single point is computed as the average of the FWHM of a horizontal and vertical profile through the point. It is well known that the tangential resolution varies quite differently from the radial resolution in a single transaxial slice. The averaging of two profiles and across points at different azimuthal angles results in a figure which characterizes the system's overall average resolution.

B. Analytical Simulations

Next, we performed analytical simulations of fully 3-D data from a whole-body phantom to evaluate the bias versus noise tradeoffs [22]. This phantom contains 24 spherical lesions of 1, 2, and 3 cm diameters and with two lesion to background ratios (3.5:1 and 1.5:1). The lesions were positioned in various background levels of the lung, thorax and liver region with an activity concentration ratio of 1:2:6, respectively. The phantom size is equivalent to a person with a 35-in waistline. Analytical projections through this phantom (emission and transmission scans) were blurred with a four-dimensional (4-D) function to simulate the nonidealities of the detection system. We used a 4-D function which blurred in s and z and was variant with radial and axial location as opposed to the 3-D system response used in reconstruction. This dimension mismatch was chosen to test the validity of the reduction in dimensionality of the system model. We also added slight variations in the 4-D model used for data simulation from the 3-D function used in the reconstruction to account for the possible inaccuracies in modeling of the system response.

We generated 50 independent realizations from this phantom with typical clinical noise levels such that each FOV contained 110 million events with 30% true, 30% scattered, and 40% randoms events. We performed attenuation correction of the 3-D data, Fourier rebinding, and then reconstructed with 2-D FBP, (AW)OSEM, and (AW)OSEM with the modified SRFs. The (AW) prefix indicates a method that decorrects the rebinned data for attenuation to enforce proportionality between the mean and variance of the data necessary for the expectation maximization (EM) algorithm [12]. The 2-D attenuation correction factors are then incorporated into the system matrix. In the following text, the (AW)OSEM methods will be denoted as OSEM for simplicity.

We analyzed these reconstructions with multiple figures of merit including the total root mean square error (rmse) computed on a voxel-by-voxel basis as defined by

$$\mathrm{rmse} = \sqrt{\sum_{i=1}^{M} \frac{\left(x_i^T - \hat{x}_i\right)^2}{M}} \tag{3}$$

where M is the number of voxels in the true image volume x^T and $\hat{x}_i$ is the ith voxel of the reconstructed image. Along with the total rmse, we also compute the rmse of tumor regions and of background regions. The tumor regions contain all voxels fully inscribed in the tumor and the background region contains all voxels in the body that are not adjacent to a tumor. To further evaluate the quantitative accuracy of reconstructed tumor volumes, we find the average bias in the maximum values of the tumor regions. This bias is computed over the $r = 1$ to R independent reconstructions as

$$\mathrm{Bias}_{\max} = \frac{1}{R * N} \sum_{i=1}^{N} \sum_{r=1}^{R} \frac{T_i - V_{\max,r,i}}{T_i} \tag{4}$$

where $N = 24$ is the number of tumors, $V_{\max,r,i}$ is the maximum value of the i tumor region in the r reconstruction, and T_i is the value of the i region in the true image. The maximum value is often used clinically for determining standardized uptake values in quantitative studies. Finally, we evaluated the average bias in the mean values of the tumor regions which is computed in a similar manner as (4) but with $V_{\mathrm{mean},r,i}$ the mean of the values in tumor region i in place of $V_{\max,r,i}$.

C. Measured Phantom

We tested the simulated system response function with measured data from a GE Advance scanner. We scanned the NEMA IEC Body Phantom consisting a large semi-cylindrical chamber containing six smaller spheres with diameters 10, 13, 17, 22, 28, and 37 mm [23]. The all spheres in the phantom were filled with F18 to have an 8:1 sphere to background activity concentration ratio. Data were collected from the phantom for 5 min in one bed position with a total of 3×10^7 events. The data were fully corrected in the 3-D domain and Fourier rebinned prior to reconstruction with our custom reconstruction package. The

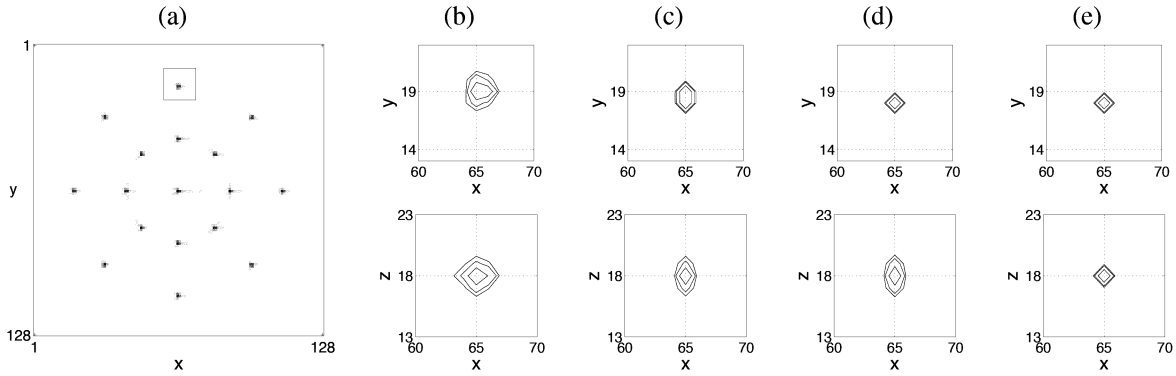

Fig. 4. Reconstruction of Monte Carlo simulations of simple phantom with point sources at 0, 10, and 20 cm from center of FOV. FBP reconstructions shown in (a) has square drawn around point with a zoomed contour view of the FBP reconstruction (b), conventional OSEM (c), OSEM + $\mathbf{S}_{1+1}$ (d), and OSEM + $\mathbf{S}_{2+1}$ (e). First row of (b)–(e) shows a transaxial slice through the point and second row shows an axial slice through the same point.

OSEM reconstructions used 13 iterations with 12 subsets and were postsmoothed with a 5-mm Gaussian filter. We evaluated the bias in the mean of the sphere values for a single reconstruction as defined as

$$\text{Bias}_{\text{mean,single,i}} = \frac{\tilde{T} - \tilde{V}_{\text{mean},i}}{\tilde{T}} \tag{5}$$

where $\tilde{V}_{\text{mean},i}$ is the mean of voxels in sphere i determined by matching spherical volumes of interest placed on all reconstructions. The "true" value $\tilde{T}$ of the sphere regions in the reconstructed image of the NEMA Body phantom is defined as eight times the mean of the background activity.

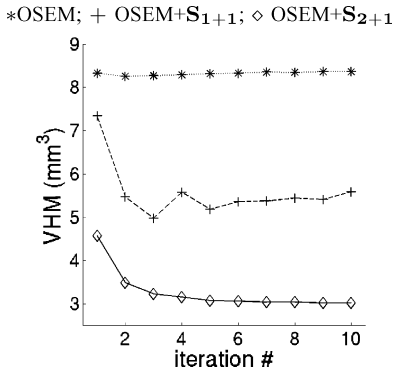

Fig. 5. Average volume with values greater than half the maximum of the reconstructed point (VHM) for each point source plotted versus iteration number to find appropriate number of iterations to perform resolution analysis with Monte Carlo simulated data.

VI. Results

A. Monte Carlo Simulations

Fig. 4 presents the image reconstruction results from the point source phantoms using FBP, conventional OSEM, OSEM + $\mathbf{S}_{1+1}$, and OSEM + $\mathbf{S}_{2+1}$. The contour plots show the shape of a reconstructed point source located at $s_v = 20$ cm in the transverse and axial plane. These contour lines mark the half maximum, fifth maximum, and tenth maximum level in each slice. The plots reveal that the use of the SRF improves the resolution at the edges of the FOV. As expected, the use of the $\mathbf{S}_{2+1}$, which includes the axial blurring component, leads to better axial resolution than the $\mathbf{S}_{1+1}$, which ignores axial effects.

The appropriate number of iterations for OSEM in this example was determined by testing the average VHM of all the point sources at each iteration of OSEM. Fig. 5 plots these values and shows that the methods using the modified SRF require more iterations to stabilize. This behavior is expected considering the SRF methods use a modified system matrix which is a blurred version of the conventional geometric system matrix, essentially resulting in a more ill-posed inverse problem. That is, the blurred system matrix compared to the conventional system matrix basically relates each voxel to more projections requiring more iterations to reach a final image.

Fig. 5 also shows that all methods converge to constant size volumes within six iterations. The OSEM algorithm applied to this simple phantom "converges" to a final image because of the nonnegativity constraint enforced during each iteration and the multitude of zero-valued projections since there is no background activity. In general, OSEM is not proven to converge and will result in different resolution properties for different emission objects. The results presented here are not intended to show the final resolution of the proposed OSEM methods, but rather to show the resolution gains in comparison to conventional OSEM with this phantom and more importantly to test the spatial variance in the resolution.

Figs. 6 and 7 present a more systematic analysis of the resolution improvements. Fig. 6 shows the transaxial FWHM and FWTM versus the radial distance from the center of the FOV for the different reconstruction methods. For this object, the two proposed methods yield an approximately 10% improvement in transaxial resolution over conventional OSEM at locations away from center of FOV. Fig. 7 presents a volumetric resolution comparison displaying the radius of the sphere inscribed in the half and tenth maximum of the points at varying radial distance. The use of the complete $\mathbf{S}_{2+1}$ results in virtually no spatial variance in resolution; or, in other words, the resolution does not change at different locations in the image. These results show that the new methods improve the resolution by as much as 20% over OSEM for image locations near the edge of the FOV.

In these plots, the resolution of the OSEM + $\mathbf{S}_{1+1}$ appears worse than conventional OSEM at the center of the FOV ($s_v =$

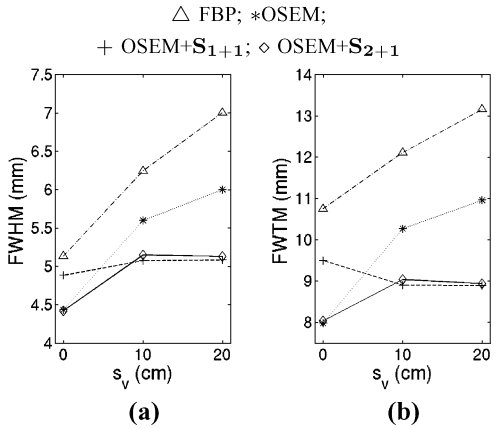

Fig. 6. (a) Average transaxial FMHM and (b) tenth maximum of the reconstructed point sources.

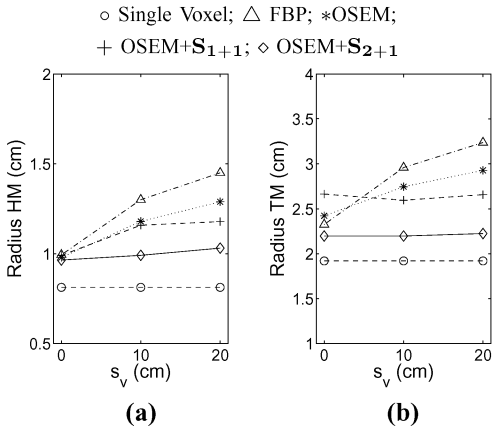

Fig. 7. Volumetric figures for resolution analysis. Average radius of a sphere inscribed in the (a) half maximum (HM) and (b) tenth maximum (TM) of each point source is plotted versus radial location. Resolution of the OSEM + SRF methods is spatially variant throughout the FOV.

0 cm). These metrics at the center of the FOV are computed from a single point where the values at the other radial locations are averaged over eight points leading to more error in the resolution metrics at the center. Also, the use of our system response function which blurs the conventional system matrix can be challenging at the center of the FOV. The response function is found in the second half of the transaxial FOV from a reversed (in radial bin) version of the response at positive radial locations. In theory, the radial system response at the center of the field of view is a symmetric function which when reversed to form kernels for the negative radial locations will be the same function. In reality, the radial response at the center of the FOV is slightly asymmetric leading to a greater transition in the system matrix at the center resulting in slight degradations at the center of the FOV. Simple smoothing of the response at the center of the FOV will remove these degradations. This minor effect is not evident with the $\mathbf{S}_{2+1}$ function since the additional axial component reduces the transition at the center of the blurred system matrix.

B. Analytical Simulations

The following results use analytically simulated data with clinically relevant noise levels as discussed in the previous

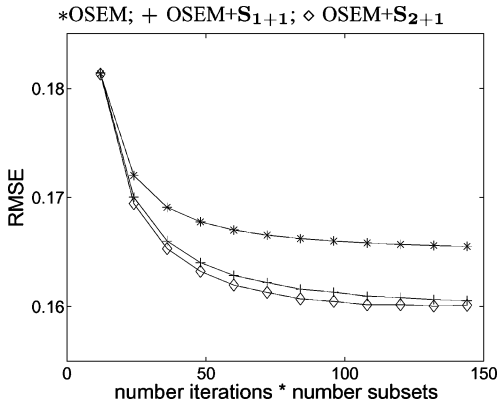

Fig. 8. Total rmse at each iteration number for whole body phantom with varying OSEM methods to determine stopping iteration number. Since OSEM does not necessarily converge, the total rmse was used to determine the number of iterations required to reach an estimate that does not change appreciably with more iterations.

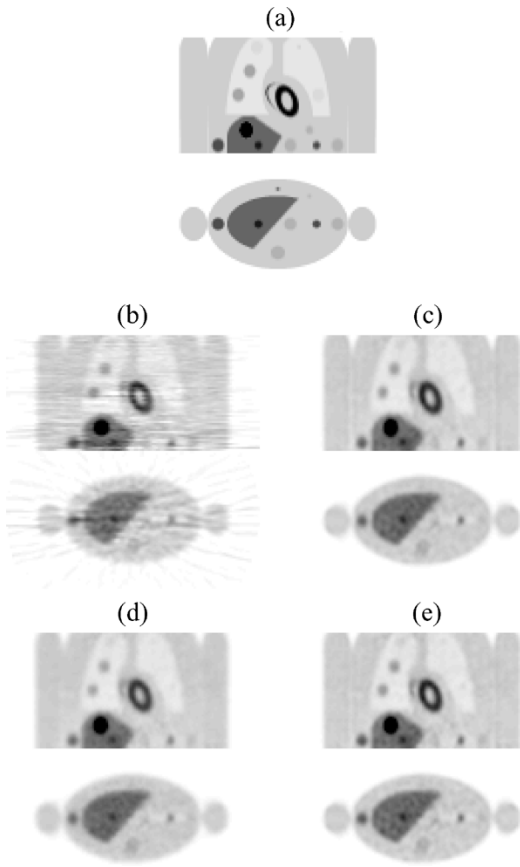

Fig. 9. Coronal and transverse slices through sample reconstructions from analytically simulated fully 3-D data of a phantom containing 24 spherical lesions of 1, 2, and 3 cm diameters and varying contrast levels (3.5:1 and 1.5:1). OSEM reconstructions (c–e) post smoothed with 3-D 10-mm Gaussian filter and FBP (b) used a 10 mm cutoff Hanning window. (a) True image. (b) FBP. (c) OSEM. (d) OSEM + $\mathbf{S}_{1+1}$. (e) OSEM + $\mathbf{S}_{2+1}$.

section. Before analyzing resolution versus noise tradeoffs, we tested the total rmse of the reconstructions at each iteration of OSEM to determine an appropriate number of iterations. Fig. 8 plots these terms and shows that the use of the SRF requires slightly more iterations than conventional OSEM to reach a stable rmse value. For this study, we used 12 subsets

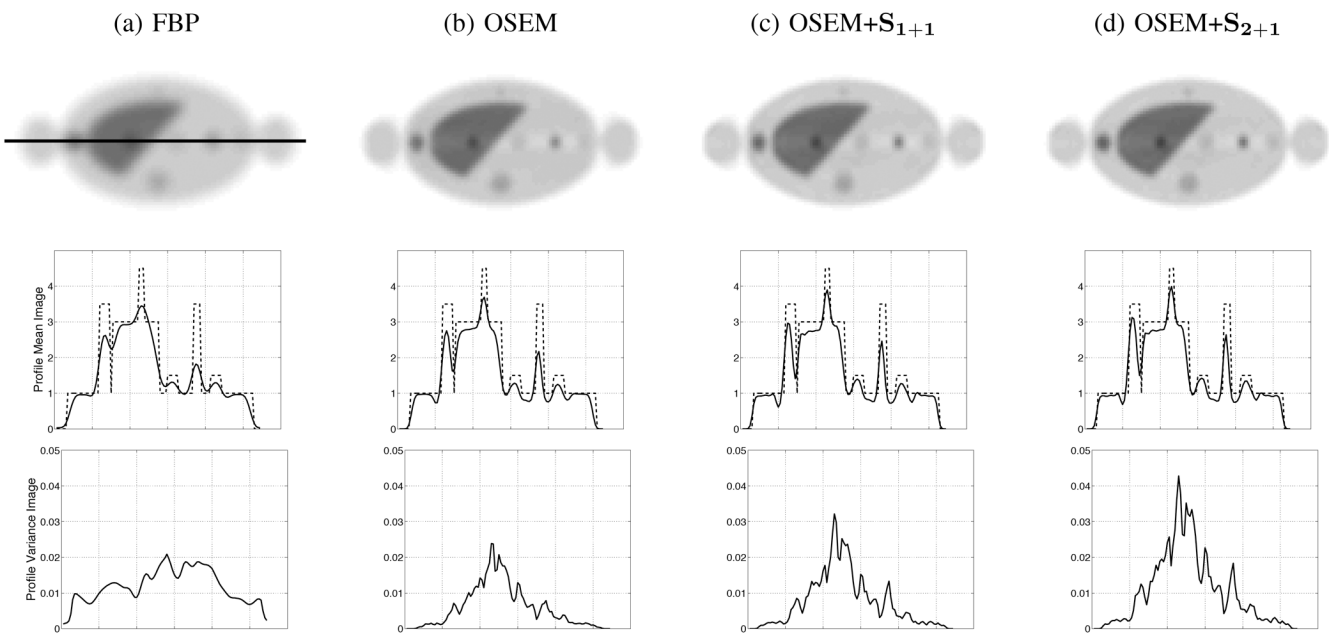

Fig. 10. Transaxial slice through mean images of 50 noise realizations. Second row plots a horizontal profile through the slice with a solid line and the profile through the true object with a dotted line. The third row presents the profile through the variance image of the 50 reconstructions of different noise realizations using the same smoothing parameter. (a) FBP. (b) OSEM. (c) OSEM + $\mathbf{S}_{1+1}$. (d) OSEM + $\mathbf{S}_{2+1}$.

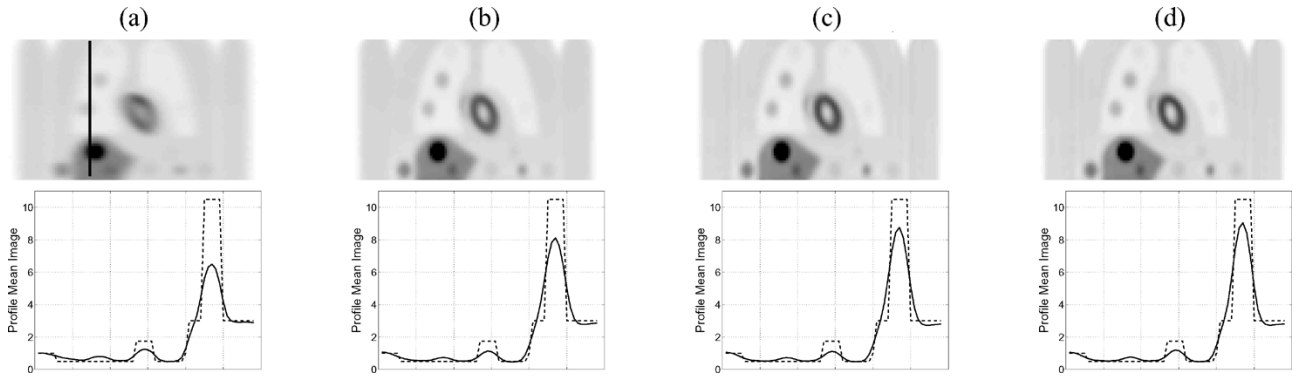

Fig. 11. Coronal slice through mean images of 50 noise realizations. Second row plots a horizontal profile through the slice with a solid line and the profile through the true object with a dotted line. (a) FBP. (b) OSEM. (c) OSEM + $\mathbf{S}_{1+1}$. (d) OSEM + $\mathbf{S}_{2+1}$.

and stopped OSEM at seven iterations, OSEM + $\mathbf{S}_{1+1}$ at nine iterations and OSEM + $\mathbf{S}_{2+1}$ at 13 iterations.

Fig. 9 shows the true image and sample reconstructions from simulated data from the whole-body phantom. It is difficult to draw conclusions from a visual assessment of a single reconstructed volume. After close inspection, one could argue that the low activity (1.5:1 tumor to background ratio) 3-cm lesion in the apex of the right lung is more visible in the proposed OSEM methods with the system model than in the conventional reconstruction methods. Moreover, the low activity smaller lesions in the left lung are only visible in the OSEM + $\mathbf{S}_{2+1}$ reconstruction.

Mean images of reconstructions of the 50 independent data sets offer insight into the accuracy of methods without confounding noise. Fig. 10 shows a transaxial slice through the mean image and plots a profile through this slice. The smoothing parameters for these reconstructions were chosen to have visually comparable noise levels. The FBP reconstruction used a 10-mm Hanning window and the OSEM methods were all postsmoothed with a 10-mm 3-D Gaussian filter. These settings reflect the common whole-body protocol in our clinic. The profile (second row) shows that the use of the SRF improves the accuracy in the tumor regions. The 2 + 1 SRF results in little discernible improvements over the 1 + 1 SRF method in this transaxial profile. This can be expected considering the 2 + 1 SRF offers additional improvements in the axial dimension and has the same response as the 1 + 1 SRF in the transaxial plane. The bottom row of Fig. 10 is a profile through the transaxial slice of the variance image of the 50 reconstructions showing that the bias improvements come at the expense of increased variance. Fig. 11 presents the same series of data for a coronal slice through the image volume. Considering that the 2 + 1 SRF blurs in the axial dimension, one might expect these profiles to show highly favorable axial performance with the 2 + 1 SRF. On the contrary, the 2 + 1 SRF offers only slightly better quantitative accuracy than the 1 + 1 SRF.

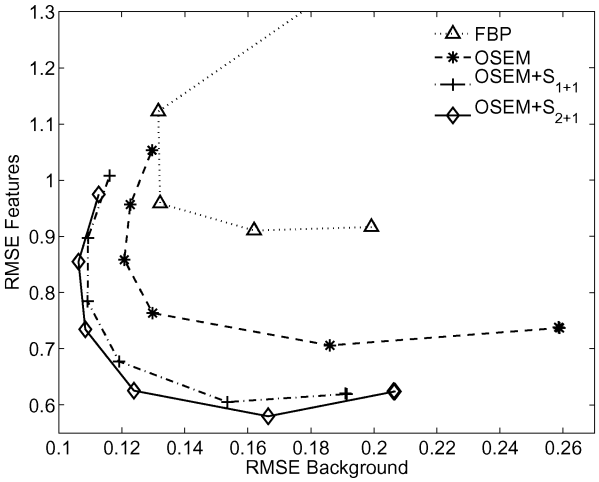

Fig. 12. Measure of accuracy comparing the rmse of the tumor regions versus the rmse of the background regions for varying smoothing parameters.

Fig. 12 presents a figure of merit describing the accuracy of the different reconstruction methods at varying smoothing parameters. For FBP, the cutoff frequency of the Hanning window was varied from 100% to 20% in 20% increments. For the OSEM methods, the postreconstruction smoothing filter was varied from no smoothing to a 15-mm Gaussian filter in 2.5 mm increments. The rmse of the tumor regions versus the rmse of the background region provides information about the error in the tumors at different noise levels. Each datum point in Fig. 12 is calculated from 50 volume images and is the average over all 24 tumors in the phantom. The statistical methods all offer images with less error than FBP and the use of the SRF provides improvement over conventional OSEM. The use of the $2 + 1$ SRF results in error only slightly less than the $1 + 1$ SRF.

Fig. 13 plots results directly linked to quantitative accuracy. The top plot in Fig. 13 shows the average bias in the maximum values of the tumor regions versus the variance in these values for different smoothing parameters. The bottom plot is the average bias in the mean value of the tumor regions versus the variance of these values. Once again, the statistical methods outperform FBP. A vertical dotted line is plotted through the FBP with a 10-mm Hanning filter to provide a frame of reference. At this noise level (which is common for the detection task), the OSEM with SRFs outperform OSEM (and FBP). The use of the $\mathbf{S}_{2+1}$ offers only slight improvements over OSEM + $\mathbf{S}_{1+1}$ in the bias of the mean values.

C. Measured Phantom

Fig. 14 presents reconstructions of the NEMA Body Phantom. All of these OSEM reconstructions were postsmoothed with a 5-mm Gaussian and shown to have a matching background voxel standard deviation to ensure a fair comparison among methods. Fig. 15 plots the bias in the mean of the spheres versus sphere diameter. The proposed methods offer reduced bias for all sphere sizes. The OSEM + $\mathbf{S}_{1+1}$ method results in images with a bias approximately 10% less than conventional OSEM and OSEM + $\mathbf{S}_{2+1}$ results in a bias approximately 21% less than conventional OSEM.

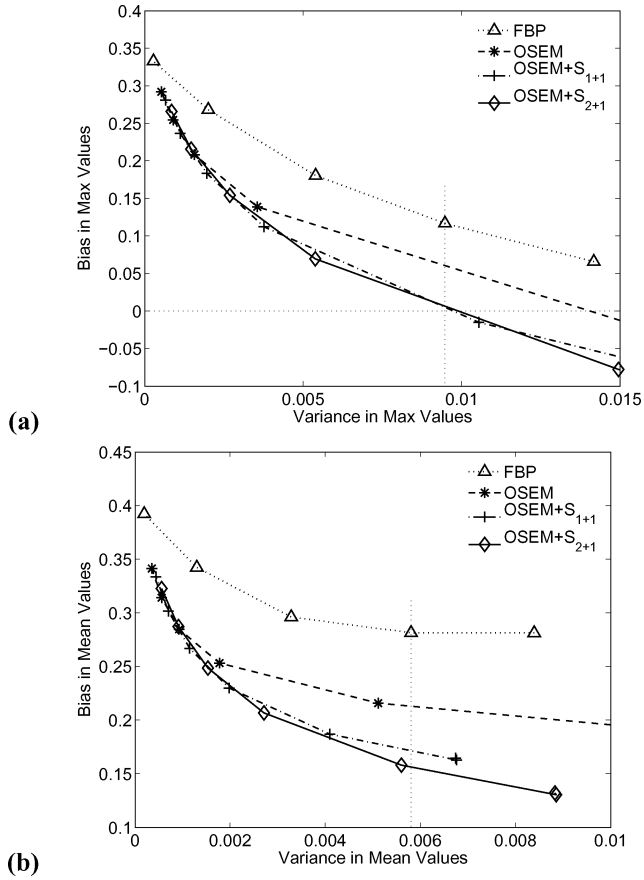

Fig. 13. Average bias in the (a) maximum value and (b) mean value of tumor region of interest versus variance in these values averaged over all 24 tumors. Curves formed from varying smoothing parameter of the reconstruction method. Vertical dotted line intersects the FBP with 10-mm Hanning cutoff filter to provide a frame of reference for the expected noise levels in the images.

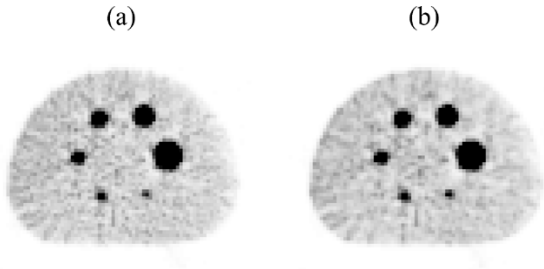

Fig. 14. Transaxial slice through reconstructions of measured NEMA Body Phantom showing (a) conventional OSEM and (b) OSEM + $\mathbf{S}_{2+1}$.

VII. Discussion

The proposed methods were implemented in our nonoptimized reconstruction code. In the current application with a 9 $\times$ 5 kernel $\mathbf{S}_{2+1}$ function applied to the conventional system matrix, the resulting system matrix has the potential of having up to 45 times the number of nonzero entries. This will substantially increase reconstruction time because of the need to compute more contributing projections from each voxel (or vice versa) during each forward/back projection operation. To offer a sense of the added computation time, we compare the reconstruction time for 64 128 $\times$ 128 images from 64 slices of 142 $\times$ 168 projection data on a 1-GHz Macintosh PowerPC G4

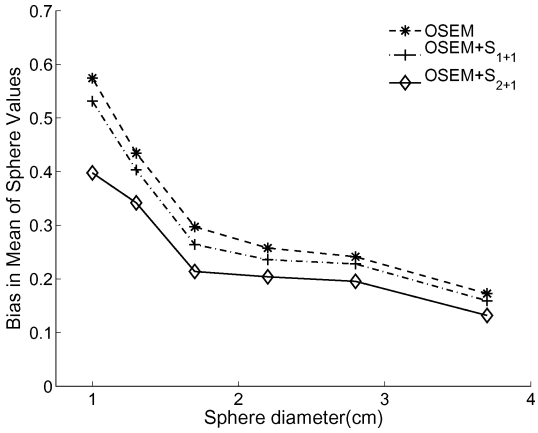

Fig. 15. Quantitative accuracy of each feature in NEMA IEC Body Phantom shown as the error in the mean values in each sphere.

with 1 GB of RAM. Conventional OSEM performs one iteration through 64 slices in 0.9 min. The OSEM + $\mathbf{S}_{1+1}$ method requires 2.5 min/iteration and the OSEM + $\mathbf{S}_{2+1}$ method requires 10.8 min per iteration. The proposed method takes 12 times as long as conventional OSEM to perform one iteration. It should be stressed that our current implementation is not optimized for speed and further work using a factorized system model and improved buffering techniques are expected to improve the reconstruction speed.

The use of a spatially variant system model with OSEM provides improved reconstructions both in terms of resolution and quantitative accuracy. As expected, the resolution improvements are more significant away from the center of the FOV and both methods lead to desirable spatially invariant resolution responses. Simulation studies show reduced variations in resolution at positions up to 20 cm from the center of the transaxial FOV. As the patient population grows in girth, transaxial uniformity at distances greater than 20 cm becomes an even more important consideration, further justifying the clinical use of the proposed methods.

Simulation and measured studies show that both proposed methods reduce rmse and tumor region bias compared to conventional algorithms. The quantitative benefits depend on tumor size and the smoothing parameter. The results from the measured NEMA IEC Body Phantom show quantitative benefits with both proposed methods and reveal that the $2 + 1$ SRF improves the accuracy over the $1 + 1$ SRF by approximately 10. In contrast, the analytical simulations showed that the quantitative accuracy of the two proposed methods are comparable with only slight benefits to using the more accurate $2 + 1$ SRF. The analytical simulations used multiple reconstructions over many smoothing parameters providing a more rigorous analysis of the quantitative benefits of the proposed methods. These simulation results suggest that the added complexity of the $2 + 1$ SRF is not warranted and that it is justifiable to use only the $1 + 1$ SRF for reconstruction of rebinned data. These findings can be appreciated in the context of Fig. 3, which reveals that the radial component is greater than the axial component. These methods need to be extended to fully 3-D iterative reconstruction methods to determine their efficacy and the tradeoffs of using response functions with more dimensionality.

VIII. Conclusion

The system response modeling in this work was performed with Monte Carlo simulations and applied to reconstructions of simulated and measured data. The proposed methods using spatially variant system models improve the resolution of conventional OSEM by as much as 20% and improve the quantitative accuracy by approximately 20% when image noise levels are set in the detection task range. The favorable results shown here will motivate our future efforts to measure the response on a real system with the approach proposed in Section III.

Acknowledgment

The authors are thankful for image reconstruction conversations with J. Fessler and system modeling conversations with M. Defrise, C. Comtat, and L. Janeiro. The authors are grateful for the constructive comments from reviewers.

References

[1] T. DeGrado, T. Turkington, J. Williams, C. Stearns, J. Hoffman, and R. Coleman, "Performance characteristics of a whole-body PET scanner," *J. Nucl. Med.*, vol. 35, no. 8, pp. 1398–1406, 1994.

[2] T. Frese, N. C. Rouze, C. A. Bouman, K. Sauer, and G. D. Hutchins, "Quantitative comparison of FBP, EM, and Bayesian reconstruction algorithms for the IndyPET scanner," *IEEE Trans. Med. Imag.*, vol. 22, no. 2, pp. 258–276, Feb. 2003.

[3] J. Qi, R. M. Leahy, S. R. Cherry, A. Chatziioannou, and T. H. Farquhar, "High-resolution 3-D Bayesian image reconstruction using the microPET small-animal scanner," *Phys. Med. Biol.*, vol. 43, no. 4, pp. 1001–1013, 1998.

[4] D. Schmitt, B. Karuta, C. Carrier, and R. Lecomte, "Fast point spread function computation from aperture functions in high-resolution positron emission tomography," *IEEE Trans. Med. Imag.*, vol. 7, no. 1, pp. 2–12, Jan. 1988.

[5] J. R. Stickel and S. R. Cherry, "High-resolution PET detector design: Modeling components of intrinsic spatial resolution," *Phys. Med. Biol.*, vol. 50, no. 2, p. 179, 2005.

[6] Y. Yang, Y.-C. Tai, and S. Siegel *et al.*, "Optimization and performance evaluation of the microPET II scanner for *in vivo* small-animal imaging," *Phys. Med. Biol.*, vol. 49, no. 12, pp. 2527–2545, 2004.

[7] K. Lee, P. E. Kinahan, J. A. Fessler, R. S. Miyaoka, and T. K. Lewellen, "Pragmatic image reconstruction for the mices fully-3-D mouse imaging pet scanner," presented at the IEEE Nucl. Sci. Symp. Med. Imag. Conf., Portland, OR, 2003.

[8] K. Lee, P. E. Kinahan, J. A. Fessler, R. S. Miyaoka, M. Janes, and T. K. Lewellen, "Pragmatic fully 3-D image reconstruction for the MiCES mouse imaging PET scanner," *Phys. Med. Biol.*, vol. 49, no. 19, pp. 4563–4578, 2004.

[9] M. Defrise, P. Kinahan, D. Townsend, C. Michel, M. Sibomana, and D. Newport, "Exact and approximate rebinning algorithms for 3-D PET data," *IEEE Trans. Med. Imag.*, vol. 16, no. 2, pp. 145–158, Feb. 1997.

[10] G. Boning, B. Pichler, M. Rafecas, E. Lorenz, M. Schwaiger, and S. Ziegler, "Implementation of Monte Carlo coincident aperture functions in image generation of a high-resolution animal positron tomograph," *IEEE Trans. Nucl. Sci.*, vol. 48, no. 3, pp. 805–810, Jun. 2001.

[11] V. Selivanov, Y. Picard, J. Cadorette, S. Rodrigue, and R. Lecomte, "Detector response models for statistical iterative image reconstruction in high resolution PET," *IEEE Trans. Nucl. Sci.*, vol. 47, no. 3, pp. 1168–1175, Jun. 2000.

[12] X. Liu, C. Comtat, C. Michel, P. Kinahan, M. Defrise, and D. Townsend, "Comparison of 3-D reconstruction with 3-D-OSEM and with FORE+ OSEM for PET," *IEEE Trans. Med. Imag.*, vol. 20, no. 8, pp. 804–814, Aug. 2001.

[13] D. Strul, R. B. Slates, M. Dahlbom, S. R. Cherry, and P. K. Marsden, "An improved analytical detector response function model for multilayer small-diameter PET scanners," *Phys. Med. Biol.*, vol. 48, no. 8, pp. 979–994, 2003.

[14] Z. Liang, "Detector response restoration in image reconstruction of high resolution positron emission tomography," *IEEE Trans. Med. Imag.*, vol. 13, no. 2, pp. 314–321, Jun. 1994.

[15] S. Staelens, Y. D'Asseler, S. Vandenberghe, M. Koole, I. Lemahieu, and R. V. D. Walle, "A three-dimensional theoretical model incorporating spatial detection uncertainty in continuous detector PET," *Phys. Med. Biol.*, vol. 49, no. 11, pp. 2337–2350, 2004.

[16] E. Mumcuoglu, R. Leahy, S. Cherry, and E. Hoffman, "Accurate geometric and physical response modeling for statistical image reconstruction in high resolution PET," in *Proc. IEEE Nucl. Sci. Symp. Med. Imag. Conf.*, 1996, vol. 3, pp. 1569–1573.

[17] E. Veklerov, J. Llacer, and E. Hoffman, "MLE reconstruction of a brain phantom using a Monte Carlo transition matrix and a statistical stopping rule," *IEEE Trans. Nucl. Sci.*, vol. 35, no. 1, pp. 603–607, Feb. 1998.

[18] E. De Bernardi, F. Zito, L. Michelutti, L. Mainardi, P. Gerundini, and G. Baselli, "Improving PET image spatial resolution by experimental measurement of scanner blurring properties," in *Proc. Eng. Med. Bio. Soc.*, 2003, vol. 1, pp. 975–977.

[19] V. Panin, F. Kehren, C. Michel, and M. Casey, "Fully 3-D PET reconstruction with system matrix derived from point source measurements," in *Proc. 8th Int. Meeting Fully 3-D Image Recon. Radiol. Nucl. Med.*, 2005, pp. 421–425.

[20] T. Lewellen, R. Harrison, and S. Vannoy, "The SimSET program in Monte Carlo calculations," in *Monte Carlo Calculations Nucl. Med.*, M. Ljungberg, S. Strand, and M. King, Eds. Philadelphia, PA: IOP, 1998, pp. 77–92.

[21] H. Hudson and R. Larkin, "Accelerated image reconstruction using ordered subsets of projection data," *IEEE Trans. Med. Imag.*, vol. 13, no. 4, pp. 601–609, Apr. 1994.

[22] C. Comtat, P. Kinahan, M. Defrise, C. Michel, C. Lartizien, and D. Townsend, "Simulating whole-body PET scanning with rapid analytical methods," in *Proc. IEEE Nucl. Sci. Symp.*, Seattle,, WA, Oct. 24–30, 1999, vol. 3, pp. 1260–1264.

[23] M. E. Daube-Witherspoon, J. S. Karp, and M. E. Casey *et al.*, "PET performance measurements using the NEMA NU 2-2001 standard," *J. Nucl. Med.*, vol. 43, no. 10, pp. 1398–1409, 2002.